COMPUTATION OF HOMOCLINIC ORBITS IN PARTIAL DIFFERENTIAL EQUATIONS: AN APPLICATION TO CYLINDRICAL SHELL BUCKLING.

G. J. LORD*, A. R. CHAMPNEYS* AND G. W. HUNT†

Abstract. This paper concerns numerical computation of localised solutions in partial differential equations (PDEs) on unbounded domains. The application is to the von Kármán–Donnell equations, a coupled system of elliptic equations describing the equilibrium of an axially compressed cylindrical shell. Earlier work suggests that axially-localised solutions are the physically prefered buckling modes. Hence the problem is posed on a cylindrical domain that is unbounded axially and solutions are sought which are homoclinic in the axial variable and periodic circumferentially.

The numerical method is based on a Galerkin spectral decomposition circumferentially to pose ordinary differential equations (ODEs) in the unbounded co-ordinate. Methods for location and parameter continuation of homoclinic solutions of ODEs are then adapted, making special use of the symmetry and reversibility properties of solutions observed experimentally. Thus a formally well-posed continuation problem is reduced to a rotational subgroup circumferentially and posed over a truncation of the half-interval axially. The method for location of solutions makes use of asymptotic approximations where available. More generally, an adaptation of the 'successive continuation' shooting method is used in the lowest possible number of circumferential modes, followed by additional homotopies to add more modes by continuation in the strength of nonlinear mode-interaction terms.

The method is illustrated step-by-step to produce a variety of homoclinic solutions of the equations and compute their bifurcation diagrams as the loading parameter varies. All computations are performed using AUTO. The techniques illustrated here for the von Kármán–Donnell equations are applicable to a wider class of PDEs.

Key words. homoclinic orbits, cylindrical shells, Galerkin approximation, initial approximations, boundary value problem

AMS subject classifications. 35J55, 65N35, 58F39, 58F05, 73C50, 73K15

1. Introduction. In recent years there has been a great deal of interest in computing connecting orbits (homoclinic or heteroclinic orbits) in dynamical systems defined by ordinary differential equations (ODEs). The key idea behind the direct numerical methods for computing homoclinic orbits to equilibria is to pose a boundary-value problem (BVP) on a truncated interval and then use the linearization about the equilibrium to define boundary conditions with the correct asymptotic behaviour [4, 20]. These techniques have been applied to great effect in small ODE systems (see, e.g. [9]) and have been specialized to Hamiltonian [4] and reversible systems [11]. Recently there have also been a number of papers on the related problem of computing homoclinic solutions to periodic orbits, see for example Beyn [5], Bai *et al* [2] and Champneys and Lord [10].

Although the techniques for continuing homoclinic solutions are now quite well developed, a key problem is locating an initial approximation. One technique is to use a shooting method, which involves solving an initial value problem to find a solution of the correct form. This has been particularly effective for small systems of ODEs or in larger systems where the unstable manifold is one-dimensional, or a solution occurs in some restricted subspace such as in [3]. However, in general, this approach is not

* Department of Engineering Mathematics, University Walk, University of Bristol, Bristol, BS8 1TR, U.K. G.J.Lord@bristol.ac.uk, A.R.Champneys@bristol.ac.uk

†School of Mechanical Engineering, University of Bath, Bath, BA2 7AY, UK. G.W.Hunt@bath.ac.uk

feasible for a large system such as that arising from the discretization of a partial differential equation (PDE). An alternative approach was used in [10] where asymptotic results were used to locate an initial approximation. In [18] a method of 'successive continuation' for finding a connecting orbit was presented with a convergence analysis and applied to a number of ODE examples (see also [14, 15]). This method, although possibly time consuming, uses continuation of an approximating sequence of BVPs as a kind of shooting method that does not suffer from the instabilities inherent in solving initial-value problems.

We also remark that [7] have solved for solutions of elliptic equations on semi-infinite domains using asymptotic boundary conditions. They found initial approximations to solutions by connecting asymptotic boundary conditions using piece-wise linear interpolation in such a way as to resemble the non-planar wavefront they sought to compute. In [23] asymptotic boundary conditions are discussed and numerical results presented for the Bratu problem, an initial approximation for Newton's method was either determined from approximating an exact solution or using the method outlined above.

We investigate a coupled system of two fourth-order elliptic PDEs, the von Kármán–Donnell equations posed on a cylindrical domain, which model the post buckling of a long thin cylindrical shell under axial compression. This is a classical problem in structural mechanics and it has long been observed experimentally that the buckling occurs locally along the axial length of the cylinder with a periodic pattern circumferentially of perhaps ten waves, depending on the radius to thickness ratio of the cylinder [19, 46]. In earlier work we confirmed numerically the existence of such solutions [32] and obtained good qualitative and quantitative agreement with experimental data. This indicates that the localization is in fact a property inherent in the perfect cylinder system.

In [32] little detail was given of the numerical method and results were presented for only one type of localised solution. In contrast, the focus of this paper is to describe in some detail the computational steps required to first *locate* and then *continue* homoclinic solutions to the von Kármán–Donnell equations. As such, our aim is that the step-by-step method used will be of practical use in computing connecting orbits in other PDE problems on infinite domains. The technique is demonstrated by computing localised solutions of a variety of types (unimodal and multi–modal, symmetric and cross-symmetric).

We consider an infinitely long cylinder and discretize the von Kármán–Donnell equations circumferentially by the Galerkin spectral method. This yields a large system of ODEs in the axial variable x, for which we seek homoclinic solutions i.e. axially localized solutions. We seek two forms of solutions to the von Kármán–Donnell equations, those which are *symmetric* axially about a section in the cylinder (see Figure 5.5) and those that are *cross-symmetric* axially (that is symmetric in even-numbered waves and anti-symmetric in odd-numbered waves, see Figure 5.4) about a section through the cylinder. Both these forms are observed experimentally [46] and can be considered as solutions that are symmetric under a reversibility of the ODEs. We are principally interested in "primary" or "uni–modal" (symmetric or cross-symmetric) homoclinic orbits. However recent work [36] strongly suggests the existence of "multi–modal" or n-pulse homoclinic orbits. These appear like n copies of the primary orbit.

Our numerical procedure is somewhat different from standard methods for computing post-buckling behaviour in shell structures (cf. [37, 38, 46]). By solving equilib-

rium equations directly rather than using the principle of virtual work, the symmetry structure of the problem is more apparent. Also for localised buckling modes, the analogy with the theory of homoclinic orbits in dynamical systems enables us to understand questions of multiplicities of solution axially far more readily and to pose the 'correct' asymptotic boundary conditions. For a comparison between finite-element and dynamical-systems based approaches for computing equilibria in a simpler structural problem, see [26]. We do, however, note that the finite-element work of [45] is similar in spirit to the present work. The approach there is to use ring-elements, that take account of the circumferential periodicity while allowing general displacements axially.

The remainder of the paper is outlined as follows. Section 2 introduces the von Kármán–Donnell equations and their Galerkin approximation. In section 3 we discuss BVP's for homoclinic orbits in conservative and reversible systems and adapt this to the von Kármán–Donnell equations, taking into account the symmetry properties of the solutions sought. In order to locate solutions at fixed parameter values, we describe in section 4 an adaptation of the successive continuation technique of [18] which exploits the existing asymptotic results on the von Kármán–Donnell equations. This procedure is illustrated with numerics. Having found an initial approximation, a homotopy technique is described for increasing the number of modes (and hence the accuracy) of the Galerkin discretization of the PDE. A further use of numerical continuation is made in changing the wave-number of the solution in the circumferential direction. Finally we suggest a simple continuation procedure to change the boundary conditions. Numerical results are presented in section 5 for the convergence of the Galerkin approximation and qualitative and quantative validity of the homoclinic solutions as localized buckling solutions. In addition we confirm numerically the existence of multi–modal solutions. All computations were performed using the numerical continuation code AUTO [16, 17]

2. The von Kármán–Donnell equations and Galerkin approximation. Here we introduce the von Kármán–Donnell equations and show how they may be treated as an example of a more general PDE problem. Existence of uni-modal (primary) and multi-modal homoclinic solutions is discussed. The Galerkin approximation is introduced and the resulting set of ODEs presented. We discuss symmetries in the problem and briefly consider numerical properties of the discretization.

2.1. The von Kármán–Donnell equations. Consider an infinitely long cylinder of radius R and shell thickness t. The classical equilibrium equations for the in–plane stress function ϕ and displacement w in the post–buckling regime of the cylinder are given by the von Kármán–Donnell equations:

$$\kappa^2\nabla^4 w + \lambda w_{xx} - \rho\phi_{xx} = w_{xx}\phi_{yy} + w_{yy}\phi_{xx} - 2w_{xy}\phi_{xy} \tag{2.1}$$

$$\nabla^4\phi + \rho w_{xx} = (w_{xy})^2 - w_{xx}w_{yy}, \tag{2.2}$$

where ∇^4 denotes the two dimensional bi–harmonic operator; $x \in \mathbb{R}$ is the axial and $y \in [0, 2\pi R)$ is the circumferential co-ordinate. The parameters appearing in (2.1) and (2.2) are the curvature $\rho := 1/R$,

$$\kappa^2 := t^2/12(1-\nu^2),$$

where ν is Poisson's ratio and the bifurcation parameter

$$\lambda := P/Et,$$

where P is the compressive axial load (force per unit length) and E is Young's modulus. The form of solutions we are concerned with suggest that equations (2.1) and (2.2) should be supplemented with periodic boundary conditions in y and asymptotic boundary conditions in the axial direction x:

$$\begin{array}{c}(w,\phi)(x,0) = (w,\phi)(x,2\pi R),\\ (w,\phi)(x,y),(w,\phi)_x(x,y),(w,\phi)_{xx}(x,y),(w,\phi)_{xxx}(x,y) \to 0 \text{ as } \ x \to \pm\infty.\end{array} \tag{2.3}$$

The von Kármán–Donnell equations (2.1-2.2) may be derived from a variational formulation for the total energy (by introducing a Lagrange multiplier), and hence the first integral I,

$$\begin{aligned} I \;=\; & \frac{Et}{2}\int\int\left\{\left(\nabla^2\phi\right)^2 - 2(1+\nu)\left[\frac{\partial^2\phi}{\partial x^2}\frac{\partial^2\phi}{\partial y^2} - \left(\frac{\partial^2\phi}{\partial x\partial y}\right)^2\right]\right\}\;dxdy \\ & + \frac{Et^3}{24(1-\nu)^2}\int\int\left\{\left(\nabla^2 w\right)^2 - 2(1-\nu)\left[\frac{\partial^2 w}{\partial x^2}\frac{\partial^2 w}{\partial y^2} - \left(\frac{\partial^2 w}{\partial x\partial y}\right)^2\right]\right\}\;dxdy \\ & - \frac{Et\lambda}{2}\int\int\left(\frac{\partial w}{\partial x}\right)^2\;dxdy \\ & - Et\int\int\phi\left\{\nabla^4\phi + \rho\frac{\partial^2 w}{\partial x^2} - \left(\frac{\partial^2 w}{\partial x\partial y}\right)^2 + \frac{\partial^2 w}{\partial^2 x}\frac{\partial^2 w}{\partial^2 y}\right\}\;dxdy \end{aligned} \tag{2.4}$$

is conserved.

We consider in this paper the von Kármán–Donnell equations (2.1-2.2) as an example of a more general PDE of the form

$$u' = Au + F(u), \tag{2.5}$$

where A is a linear operator, F is a nonlinear function, with appropriate boundary conditions on some suitable domain, unbounded in x. One way we may write (2.1), (2.2) in the form (2.5) is by defining u to be

$$u := \left(w, w_x, w_{xx}, w_{xxx}, \phi, \phi_x, \phi_{xx}, \phi_{xxx}\right)^T,$$

in which case A is given by

$$A := \begin{pmatrix} 0 & 1 & 0 & 0 & 0 & 0 & 0 & 0 \\ 0 & 0 & 1 & 0 & 0 & 0 & 0 & 0 \\ 0 & 0 & 0 & 1 & 0 & 0 & 0 & 0 \\ 0 & 0 & -(\frac{\lambda}{\kappa^2} + 2w_{yy}) & 0 & 0 & 0 & \frac{\rho}{\kappa^2} & 0 \\ 0 & 0 & 0 & 0 & 0 & 1 & 0 & 0 \\ 0 & 0 & 0 & 0 & 0 & 0 & 1 & 0 \\ 0 & 0 & 0 & 0 & 0 & 0 & 0 & 1 \\ 0 & 0 & -\rho & 0 & 0 & -2\phi_{yy} & 0 & 0 \end{pmatrix}$$

and $F(u) := (0,0,0,f_1,0,0,0,f_2)^T$ where

$$f_1 := -w_{yyyy} + \left(w_{xx}\phi_{yy} + w_{yy}\phi_{xx} - 2w_{xy}\phi_{xy}\right)/\kappa^2$$

and

$$f_2 := -\phi_{yyyy} + \left[(w_{xy})^2 - w_{xx}w_{yy}\right]/\kappa^2.$$

Systems of the form (2.5) were shown by Mielke [35] to have a Hamiltonian structure. The existence of unimodal (or primary) homoclinic orbits (also sometimes referred to as ground states) for equations of a similar form to (2.1) and (2.2) have been considered by a number of authors (see for example [44] and references therein). As the primary purpose of this paper is to present a numerical method, we shall not pursue these existence questions in detail. However, we do note the recent work by Peterhof et al. [36] which proves an exponential dichotomy result for non-degenerate primary orbits for a class of elliptic PDEs on cylindrical domains. Such a result strongly suggests the existence of multi–modal solutions whenever the equilibrium has complex eigenvalues as in [12, 8] for finite-dimensional systems.

2.2. The Galerkin approximation. We now consider the spatial discretization of the von Kármán–Donnell equations by a Galerkin approximation. The system (2.1) and (2.2) has a rich structure of symmetries, see [21, 25, 29] and [45]. In accordance with observed deformation patterns, we seek solutions that are even periodic solutions in y and which remain within the subspace corresponding to invariance under rotation through $2\pi/s$. Hence we use the following cosine functions as the basis functions in the Galerkin approximation

$$w(y) = \sum_{m=0}^{\infty} a_m \psi_m^s; \qquad \phi(y) = \sum_{m=0}^{\infty} b_m \psi_m^s,$$

where

$$\psi_m^s = \cos(ms\rho y), \qquad m \in \mathbb{N} \cup \{0\}, s \in \mathbb{N}.$$

We refer to $\psi_1^s = \cos(s\rho y)$ as the *seed mode*.

Substituting into the von Kármán–Donnell equations, taking the L^2 inner product and expanding the nonlinear terms we find the following system of ODEs

$$\begin{aligned} \kappa^2 \left\{ \frac{\partial^4 a_m}{\partial x^4} - 2s^2\rho^2 m^2 \frac{\partial^2 a_m}{\partial x^2} + s^4\rho^4 m^4 a_m \right\} + \lambda \frac{\partial^2 a_m}{\partial x^2} - \rho \frac{\partial^2 b_m}{\partial x^2} \\ = s^2\rho^2 \chi \left\{ -\frac{1}{2} \widetilde{\sum_{k,\ell,m}} \left(\ell^2 \frac{\partial^2 a_k}{\partial x^2} b_\ell + k^2 a_k \frac{\partial^2 b_\ell}{\partial x^2} \right) - {\sum_{k,\ell,m}}' k\ell \frac{\partial a_k}{\partial x} \frac{\partial b_\ell}{\partial x} \right. \\ \left. + {\sum_{k,\ell,m}}'' k\ell \frac{\partial a_k}{\partial x} \frac{\partial b_\ell}{\partial x} \right\} \end{aligned} \tag{2.6}$$

$$\begin{aligned} \frac{\partial^4 b_m}{\partial x^4} - 2s^2\rho^2 m^2 \frac{\partial^2 b_m}{\partial x^2} + s^4\rho^4 m^4 b_m + \rho \frac{\partial^2 a_m}{\partial x^2} \\ = s^2\rho^2 \frac{1}{2} \chi \left\{ \widetilde{\sum_{k,\ell,m}} \ell^2 \frac{\partial^2 a_k}{\partial x^2} a_\ell + {\sum_{k,\ell,m}}' k\ell \frac{\partial a_k}{\partial x} \frac{\partial a_\ell}{\partial x} - {\sum_{k,\ell,m}}'' k\ell \frac{\partial a_k}{\partial x} \frac{\partial a_\ell}{\partial x} \right\}, \end{aligned} \tag{2.7}$$

for $m = 0, 1, 2, \cdots, \infty$, and where

$$\chi = \begin{cases} \frac{1}{2}, & m = 0 \\ 1, & \text{otherwise.} \end{cases}$$

The summations terms in (2.6) and (2.7) are defined for a given value of m by:

$$\widetilde{\sum_{k,\ell,m}} := \sum_{\substack{k+\ell-m=0,k-\ell+m=0\\ k-\ell-m=0,\quad k,\ell\in\mathbb{N}\cup 0}} ; \qquad \sum_{k,\ell,m}' := \sum_{\substack{k-\ell+m=0,k-\ell-m=0\\ k,\ell\in\mathbb{N}\cup 0}} \qquad \sum_{k,\ell,m}'' := \sum_{\substack{k+\ell-m=0\\ k,\ell\in\mathbb{N}\cup 0}} .$$

The Galerkin approximation is formed by taking equations (2.6) and (2.7) for $m = 0, \cdots, M-1$ only, for some finite M. Taking $s = 1$ corresponds to a standard Galerkin approximation discussed, for example, in Gottlieb and Orszag [22], whereas $s > 1$ corresponds to seeking a solution in a specific subspace corresponding to the circumferential wave number s.

For the general form of PDE (2.5) we may write the Galerkin approximation U to the true solution u as $U = (U_0, U_1, \cdots, U_{M-1})^T$ where

$$U_m' = A_m U_i + F_m(U_0, U_1, \ldots, U_{M-1}), \quad m = 0, \ldots, M-1. \tag{2.8}$$

The Galerkin approximation to the von Kármán–Donnell equations may be written in this form with

$$U_m := \left(a_m, \frac{\partial a_m}{\partial x}, \frac{\partial^2 a_m}{\partial x^2}, \frac{\partial^3 a_m}{\partial x^3}, b_m, \frac{\partial b_m}{\partial x}, \frac{\partial^2 b_m}{\partial x^2}, \frac{\partial^3 b_m}{\partial x^3}\right)^T .$$

In which case $U \in \mathbb{R}^{8M}$ and each A_m is given by

$$A_m := \begin{pmatrix} 0 & 1 & 0 & 0 & 0 & 0 & 0 & 0 \\ 0 & 0 & 1 & 0 & 0 & 0 & 0 & 0 \\ 0 & 0 & 0 & 1 & 0 & 0 & 0 & 0 \\ s^4\rho^4 m^4 & 0 & 2s^2\rho^2 m^2 - \frac{\lambda}{\kappa^2} & 0 & 0 & 0 & \frac{\rho}{\kappa^2} & 0 \\ 0 & 0 & 0 & 0 & 0 & 1 & 0 & 0 \\ 0 & 0 & 0 & 0 & 0 & 0 & 1 & 0 \\ 0 & 0 & 0 & 0 & 0 & 0 & 0 & 1 \\ 0 & 0 & -\rho & 0 & -s^4\rho^4 m^4 & 0 & 2s^2\rho^2 m^2 & 0 \end{pmatrix} \tag{2.9}$$

and

$$F_m(U) := \left(0, 0, 0, \frac{1}{\kappa^2} f_a, 0, 0, 0, \frac{1}{\kappa^2} f_b\right)^T$$

where f_a and f_b are given by the right-hand side of (2.6) and (2.7) respectively.

There is a further symmetry of von Kármán–Donnell equations that plays an important role in the localised buckling solutions observed physically. The buckling modes observed experimentally, see for example [46, Fig. 3.52e/f], tend either to be *symmetric* (Figure 5.4) or *cross-symmetric* (Figure 5.5) about a horizontal cross-section of the cylinder. A solution to (2.1), (2.2) that is *symmetric* about the cross-section $x = T$ satisfies

$$w(x, y) = w(2T - x, y) \qquad \& \qquad \phi(x, y) = \phi(2T - x, y). \tag{2.10}$$

Equations (2.10) impose the natural symmetric conditions on the Fourier modes a_k and b_k (at $x = T$),

$$\frac{\partial a_m(T)}{\partial x} = 0, \frac{\partial^3 a_m(T)}{\partial x^3} = 0, \frac{\partial a_m(T)}{\partial x} = 0, \frac{\partial^3 b_m(T)}{\partial x^3} = 0 \qquad m = 0, \cdots, M-1.$$

In contrast, a *cross-symmetric* solution satisfies, about a section $x = T$ for some seed mode s, that

$$w(x,y) = w(2T - x, y + \pi R/s) \;\&\; \phi(x,y) = \phi(2T - x, y + \pi R/s). \tag{2.11}$$

In terms of the Fourier modes, constraints (2.11) are equivalent to

$$a_{2k}(2T - x) = a_{2k}(x), \qquad a_{2k+1}(2T - x) = -a_{2k+1}(x) \tag{2.12}$$

$$b_{2k}(2T - x) = b_{2k}(x), \qquad b_{2k+1}(2T - x) = -b_{2k+1}(x) \tag{2.13}$$

for $k = 0, 1, 2 \cdots$. Thus at $x = T$ we have that

$$\frac{\partial a_m(T)}{\partial x} = \frac{\partial b_m(T)}{\partial x} = \frac{\partial^3 a_m(T)}{\partial x^3} = \frac{\partial^3 b_m(T)}{\partial x} = 0, \qquad m = 0, 2, 4, \cdots;$$

$$a_m(T) = b_m(T) = \frac{\partial^2 a_m(T)}{\partial x^2} = \frac{\partial^2 b_m(T)}{\partial x^2} = 0, \qquad m = 1, 3, 5, \cdots.$$

It is not difficult to see that the symmetries of (2.1) and (2.2) defined by (2.10) and (2.11) define a *reversibility* of the ODEs (2.6) and (2.7) as in [13]. A general system, such as (2.8), is said to be reversible if there exists a transformation R such that $U(x)$ is invariant under $x \to -x$, $U \to RU$ and such that $S = \mathrm{fix}(R)$ is a sub–manifold of half the dimension of phase space. Solutions which are invariant under R then satisfy the constraint that

$$U(T) \in S. \tag{2.14}$$

For the Galerkin approximation (2.6-2.7) to the von Kármán–Donnell equations $S = \mathrm{fix}(R)$ is an $4M$–dimensional sub–manifold of phase space $\mathbb{R}^{8M}$ and we have a $4M$–dimensional constraint that $U(T) \in S$.

Note, finally, that there is a "degeneracy" in equations (2.6) and (2.7) for the zero mode ($m = 0$) such that these could be solved with initial conditions for

$$\frac{\partial^2 a_0}{\partial x^2}, \frac{\partial^3 a_0}{\partial x^3}, \frac{\partial^2 b_0}{\partial x^2}, \frac{\partial^3 b_0}{\partial x^3}$$

independently of the initial conditions for a_0, b_0 and the first derivatives. This corresponds to a trivial translational symmetry in the problem (sometimes termed a rigid body mode). Moreover, the single mode approximation found by taking $M = 1$ ($m = 0$ only) in (2.6) and (2.7) yields a linear system for which there are no homoclinic solutions. Thus the simplest approximation we can take that may admit a homoclinic solution is the two mode approximation found by taking $M = 2$ ($m = 0, 1$) in (2.6) and (2.7).

A standard periodic analysis of the von Kármán–Donnell equations seeks the minimum load $\lambda = \lambda_d$ and corresponding axial and circumferential wavelengths such that a bifurcation occurs. One may easily show in this way that $\lambda_d = 2\rho\kappa$. Wavelengths for which $\lambda = \lambda_d$ lie on a circle in axial/circumferential wave space as first elucidated by Koiter [31]. For a weakly non-linear analysis of mode interaction of solutions close to the Koiter circle for the von Kármán–Donnell equations see [27]. Interpreted in the present context, this analysis suggests that once a circumferential wave number has been chosen, then there is a small amplitude bifurcation of (a pair of) homoclinic solutions at $\lambda = \lambda_d$ as in the normal form of a Hamiltonian-Hopf bifurcation [30].

Alternatively the value λ_d at which the bifurcation occurs may be found in the standard way by considering the linearization of the von Kármán–Donnell equations about the trivial solution. This is equivalent to finding the eigenvalues of the *infinite* matrix A_M ($M = \infty$) in (2.9) with $s = 1$ and determining the values of λ when the eigenvalues cross the real axis. This occurs in the zero mode (m=0) at $\lambda = \lambda_d = 2\rho\kappa$. From this we conclude that the von Kármán–Donnell equations and Galerkin approximation share the same bifurcation point.

We note that equations (2.6) and (2.7) could equally well have been derived from the variational form (2.4) used to derive (2.1) and (2.2). So the Galerkin approximation conserves a first integral I_M which converges to that of the full variational problem I as $M \to \infty$. Finally it was noted in section 2.1 that the von Kármán–Donnell equations are a Hamiltonian system. The question remains as to whether the system of ODEs obtained from the Galerkin approximation is also Hamiltonian. In general, the Hamiltonian structure is not preserved [33], for other work on Hamiltonian methods for PDEs see [34, 43, 1, 24].

3. The homoclinic boundary-value problem and its solution. We seek homoclinic solutions to (2.6) and (2.7) truncated for some M. As already mentioned these ODEs are conservative and reversible. First we briefly review methods for constructing well-posed BVPs for homoclinic solutions to hyperbolic equilibria in ODEs of the form (2.8) that are either conservative or reversible. Then we discuss the implementation of these methods to define continuation problems for solutions to (2.6), (2.7) as λ varies. Finally we look at methods for locating solutions at fixed parameter values.

3.1. Boundary-value problems for homoclinic orbits. Consider a conservative system of ODEs dependent on a parameter $\mu \in \mathbb{R}$ of the form given by (2.8), with first integral $I_M(U, \mu) \in \mathbb{R}$. Note this does not necessarily arise from the discretization of a PDE. Homoclinic orbits to a hyperbolic steady state $\widetilde{U}$ are well approximated as the solution to the following BVP (cf. [4]).

Truncate the interval $(-\infty, \infty)$ to $(0, T)$ and re-scale to the interval $(0, 1)$. Introduce an artificial parameter μ_1 that breaks the invariance of I_M (cf. [42]), and solve the extended system for $x \in [0, 1]$

$$U_m' = T\left(A_m U_i + F_m(U_0, U_1, \ldots, U_{M-1})\right) + \mu_1 \nabla I_M(U, \mu), \tag{3.1}$$

for $m = 0, \ldots, M-1$. Note that for a solution of the conservative system (2.8) the artificial parameter μ_1 should be zero theoretically. At $x = 0, 1$ take the projection boundary conditions

$$L_s(U(0) - \widetilde{U}) = 0 \tag{3.2}$$

$$L_u(U(1) - \widetilde{U}) = 0 \tag{3.3}$$

where $L_{s,u}$ are matrices whose rows span the left eigenspace of the corresponding stable (s) and unstable (u) eigenvalues. In addition we require a phase fixing condition to be satisfied which we denote by

$$\Psi(U) = 0.$$

In the special case where the system is reversible and a homoclinic solution is sought that is invariant under the reversibility, the boundary-value problem may be simplified, see [11]. In this case, the right hand-boundary conditions (3.3) may be

replaced by a condition placing solutions in the fixed point set of the reversibility (2.14). Since (2.14) is one less constraint than (3.3) we can remove one free parameter, namely the breaking parameter μ_1.

For error estimates relating solutions of the full problem (3.1) to those of the truncated boundary value problem (3.1) we refer the reader to Beyn [4], Friedman and Doedel [20], Schecter [41] and Sandstede [39].

3.2. Specific implementation. We now discuss the implementation of the above boundary-value problem for the Galerkin approximation given by (2.6), (2.7) for a fixed value of M.

Recall from section 2 the definition of the bifurcating buckling load λ_d. For $\lambda < \lambda_d$ the linearization of (2.6), (2.7) about the trivial solution yields 4 zero eigenvalues, $(4M-2)$ eigenvalues in the left half-plane and $(4M-2)$ eigenvalues in the right half-plane. The non–zero eigenvalues occur in complex conjugate pairs. We see from the linearization that the equilibrium is not hyperbolic and instead has a centre–stable and centre–unstable manifolds. However by inspection it is clear that these the zero eigenvalues and associated directions are a consequence of the 'degeneracy' in the zero mode. Thus, although we solve for the full system we consider the reduced linear problem for computing the projection boundary conditions (3.2). The degeneracy in the zero mode forces the boundary conditions for that mode to be modified, as we now describe.

For symmetric or cross-symmetric homoclinic orbits, we seek solutions of the following BVP. Rescale (2.6, 2.7) to the interval $(0,1)$ and solve subject to

- Boundary conditions at $x = 0$ for the zero mode ($m = 0$)

$$a_0(0) = 0, \frac{\partial a_0(0)}{\partial x} = 0, b_0(0) = 0, \frac{\partial b_0(0)}{\partial x} = 0. \tag{3.4}$$

  These four conditions impose that the solution is homoclinic to the flat equilibrium state, rather than some translate of it.
- Standard projection boundary conditions of the form (3.2) for the non–zero modes ($m > 0$) at $x = 0$. This gives $4M-2$ conditions.
- Section boundary conditions at $x = 1$ given by

$$\frac{\partial^3 a_0(1)}{\partial x^3} = 0, \frac{\partial^3 b_0(1)}{\partial x^3} = 0 \tag{3.5}$$

  for the zero mode ($m = 0$), and,

$$\frac{\partial^i a_m(1)}{\partial x^i} = 0, \frac{\partial^{i+2} a_m(1)}{\partial x^{i+2}} = 0, \frac{\partial^i b_m(1)}{\partial x^i} = 0, \frac{\partial^{i+2} b_m(1)}{\partial x^{i+2}} = 0 \tag{3.6}$$

  for $m = 1, \cdots, M-1$. In (3.6) $i = 1$ for a symmetric solution. For a cross-symmetric solution $i = 0$ if m is odd and $i = 1$ if m is even. Together (3.5) and (3.6) give a further $4M-2$ boundary conditions.

In total we have $8M$ boundary conditions for $8M$ equations, which is the appropriate number for a well–posed problem. This BVP can be solved by a regular continuation code, such as AUTO [17, 16], to compute load-deflection bifurcation diagrams. Numerical results, found using the BVP described above, are presented in section 5. A harder computational problem is to locate solutions at a fixed load. It is this problem that we now address.

4. Location of an initial solution. For systems of ODEs of the form (2.8) arising from the discretisation of PDEs, a variety of techniques can be applied to locate an initial homoclinic solution for continuation. We describe those techniques which have proved useful for the von Kármán–Donnell equations and illustrate each technique with sample numerical results.

To compare with the experiments of Yamaki [46] and the asymptotic analysis of [28] all calculations were performed for a shell with

$$\rho = 0.01\text{mm}^{-1}, \qquad t = 0.247\text{mm}, \qquad \nu = 0.3, \qquad E = 5.56\text{GPa}. \tag{4.1}$$

In the figures below x is plotted on [0,2T] unless otherwise indicated and x,y,$w(x,y)$ and Fourier coefficients a_k are measured in *mm*. All computations (other than those for Figure 4.1) were performed using the numerical continuation code AUTO and, unless otherwise stated, the number of collocation intervals NTST=20.

Clearly the ideal situation is to have an analytic solution for some set of parameters; more realistically an approximate solution may be available. In [7] an initial approximation was constructed from a piece-wise linear approximation to the sought after solution. In low dimensional systems numerical shooting has proved a successful technique for finding an approximate solution, but is, in general, unsuitable for a large system of equations.

One form of approximate solution that is often available arises from an asymptotic expansion about the bifurcation point. This may either be a closed form of solution (such as used in [10]) or may require a simpler set of equations to be solved numerically.

4.1. Using asymptotic solutions. An asymptotic analysis of (2.1) and (2.2), valid for λ close to λ_d, is performed by considering a periodic form of solution with n waves in the circumferential direction and ℓ waves in the axial direction. The modal aspect ratio is then given by $\beta = n/\ell$. The first approximation to the displacement w and stress function ϕ are then given by

$$w_1 = \left[A(X)\cos(\gamma x) + C(X)\cos\beta^2\gamma x\right]\Xi_{s,c} + B(X)\cos(1+\beta^2)\gamma x \tag{4.2}$$

$$\phi_1 = \left[a(X)\cos(\gamma x) + c(X)\cos\beta^2\gamma x\right]\Xi_{s,c} + b(X)\cos(1+\beta^2)\gamma x \tag{4.3}$$

where $a = kA, b = kB, c = kC$, $k = \rho\gamma/(1+\beta^2)^2$ and $\gamma = \rho n/\beta$. X is a slow space variable defined by $X = (\lambda_d - \lambda)^{1/2}x$. For a symmetric solution $\Xi_{s,c} = \cos(\beta\gamma y)$ and for a cross-symmetric solution $\Xi_{s,c} = \sin(\beta\gamma y)$. The coefficients $A(X)$, $B(X), C(X)$ satisfy the amplitude equation

$$\begin{aligned} 8(1-\beta^2)^2k^2A'' - 2A + 3\rho\beta^2BC &= 0 \\ 16(1+\beta^2)^2k^2B'' - 4(1+\beta^2)^2B + 3\rho\beta^2AC &= 0 \\ 8(1-\beta^2)^2k^2C'' - 2\beta^4C + 3\rho\beta^2AB &= 0. \end{aligned} \tag{4.4}$$

Full details on the asymptotics may be found in [27]. Note that, even in this reduced space, shooting for homoclinic orbits to (4.4) to an equilibrium with three dimensional stable and unstable manifolds requires much ad-hoc use of numerical search routines. Moreover, there is no guarantee that the asymptotic solution will converge when substituted as an initial approximation to a solution of the full BVP.

Step 1: Shoot to find a homoclinic solution to the ODE system (4.4) for the asymptotics. In this case we sought a homoclinic solution to (4.4), symmetric about a section S in the slow space variable X (see Figure 4.1). This gives an approximate homoclinic

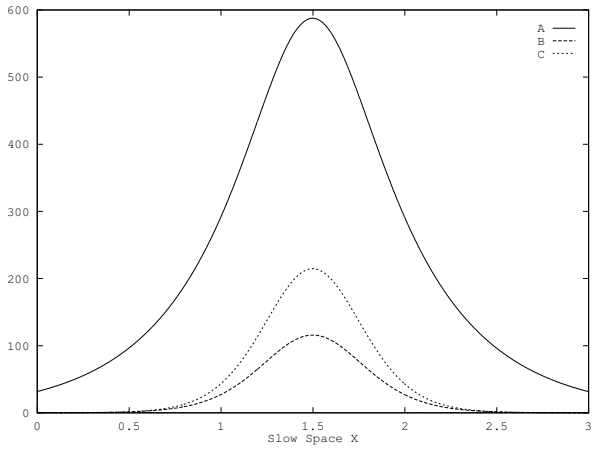

FIG. 4.1. *Homoclinic solutions to the amplitude equations* (4.4) *found by numerical shooting, plotted against the slow space variable* $X = (\lambda_d - \lambda)^{1/2}x$ *with* $\beta = 2$.

solution to the von Kármán–Donnell equation valid close to the bifurcation point λ_d. The example shown in Figure 4.1 was computed with $\beta = 2$ since approximate initial guesses for shooting were available from [27, Fig. 3]. With $\beta = 2$ the condition for the solution to lie on the Koiter circle is that $n = 15$. These were the values used to get an initial approximation. A number of different values of λ (and hence X) were taken. The length of the interval for the slow variable X over which A, B and C are solved for gives a length for the interval $[0, T]$ for the variable x.

Step 2: From equations (4.2) and (4.3) we can easily find an initial guess for the Fourier coefficients a_0, a_1, b_0, b_1, namely,

$$a_0 = B(X)\cos(1+\beta^2)\gamma x, \qquad a_1 = A(X)\cos(\gamma x) + C(X)\cos\beta^2\gamma x\Xi_{s,c}$$

and

$$b_0 = b(X)\cos(1+\beta^2)\gamma x, \qquad b_1 = a(X)\cos(\gamma x) + c(X)\cos\beta^2\gamma x\Xi_{s,c}.$$

Note that for both the symmetric and cross-symmetric case the zero modes a_0 and b_0 approximately look like a sech function modulated by a sinusoid. These initial approximations for the Fourier coefficients may be seen in Figure 4.2 with $s = 15$ and $\lambda = 8.0 \times 10^{-4}$ and $\gamma = 15\rho/2$. In (a) we have plotted a_0, a_1 and in (b) b_0 and b_1. In (c) and (d) we have reconstructed the corresponding displacement $w(x, 0)$ and stress function $\phi(x, 0)$.

Step 3: Try the initial guesses of Step 2 in AUTO as solutions to the boundary value problem (2.2–2.6), taking as a free parameter one of the problem parameters (for example λ). This was found to work in a small number of cases. For example in the cross-symmetric case with $n = 15$ (and so $s = 15$), $T = 56.86$, $\lambda = 8.0 \times 10^{-4}$ we see in Figure 4.2 the Fourier modes a_0, a_1 (a) and b_0, b_1 (b) for the asymptotic approximation and the numerical solution to the BVP (found with the asymptotic solution as an initial approximation). Note that the form and magnitude changes from the initial asymptotic approximation to the solution of the BVP and there is a correspondingly large jump in the value of the parameter λ to $\lambda = 5.035727 \times 10^{-4}$. In most cases the BVP failed to converge given an initial approximation from the

asymptotic analysis. With a failure of Step 3 we apply the method of successive continuation.

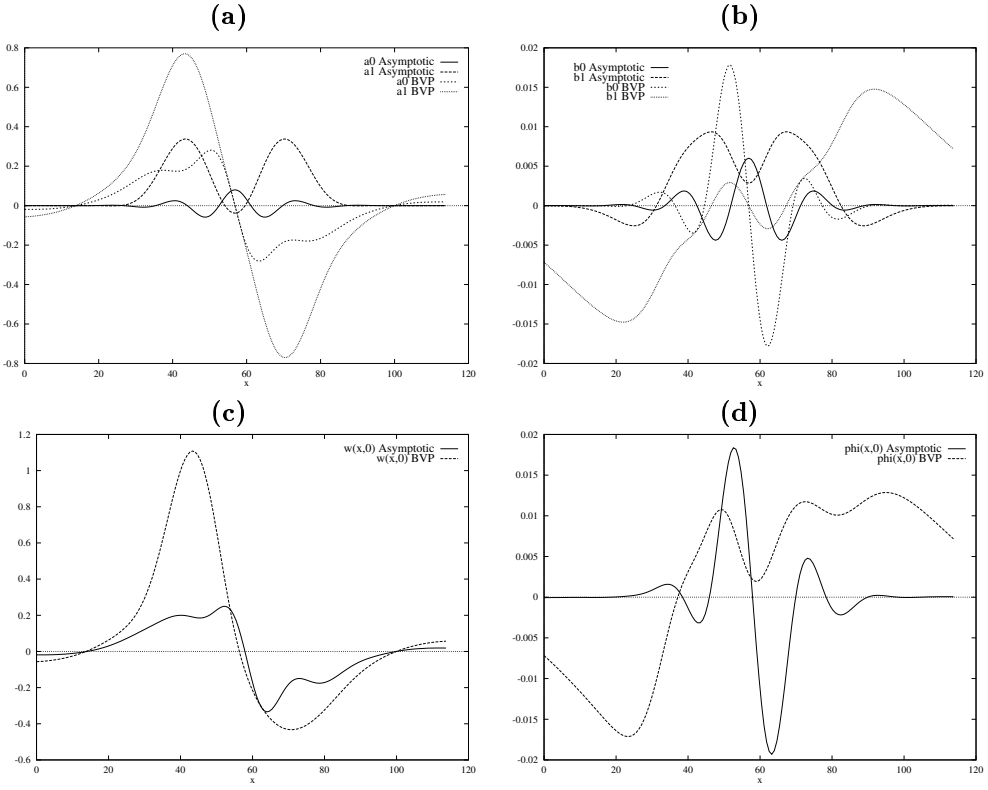

FIG. 4.2. *Figure illustrating the asymptotic solution used as an initial approximation to the BVP. Fourier modes a_0, a_1 (a) for the displacement and Fourier modes b_0, b_1 (b) for the stress function ϕ for both the initial approximation found from the asymptotics and the solution found from the BVP. Reconstructed solutions $w(x,0)$ (c) and $\phi(x,0)$ (d).*

4.2. Successive continuation. We now describe an implementation of the method described in detail in [18] (see also [15, 14] for other applications). For PDEs of the form (2.5), the method is applied to the ODEs in the lowest possible number of modes for which it is possible to obtain homoclinic solutions. For the case of the von Kármán–Donnell equations, described below, this corresponds to $M = 2$: a sixteen-dimensional system of equations.

We introduce 12 extra parameters, 6 parameters to span the unstable eigenspace at the left hand end point (at $x = 0$), and 6 parameters to parameterize the symmetric section boundary conditions (at $x = 1$). We solve (2.6, 2.7) subject to the following 22 boundary conditions, leaving 7 free parameters.

- Projection onto the unstable manifold at $x = 0$ gives 16 boundary conditions:

$$a_m(0) - \sum_{k=1}^{6} \epsilon \mu_k \psi_k = 0, \qquad m = 0, 1$$

$$b_m(0) - \sum_{k=1}^{6} \epsilon \mu_k \psi_k = 0, \qquad m = 0, 1$$

where ϵ is a fixed small parameter, ψ_k is the linear approximation to the unstable manifold at $x = 0$, and μ_k, $k = 1, \cdots, 6$, are unknown parameters.

- Symmetric or cross-symmetric section boundary conditions of the form,

$$\frac{\partial^i a_m(1)}{\partial x^i} - \alpha_k = 0 \quad k = 1, 2, 3; \quad \frac{\partial^i b_m(1)}{\partial x^i} - \alpha_k = 0 \quad k = 4, 5, 6; \tag{4.5}$$

where, for a symmetric solution,

$$i = \begin{cases} 3 & m = 0 \\ 1, 3 & m = 1 \end{cases}$$

and for a cross–symmetric solution

$$i = \begin{cases} 3 & m = 0 \\ 0, 2 & m = 1 \end{cases} .$$

This gives another 6 boundary conditions and so the problem is well posed. Taking α_k,$(k = 1, \cdots, 6)$ as free parameters the boundary conditions (4.5) are always satisfied. However to satisfy the boundary conditions given by (3.4–3.6) we require that

$$\alpha_k = 0, \qquad k = 1, \cdots, 6. \tag{4.6}$$

The other free parameter is taken to be *one* of the parameters $\mu_k, k = 1, \cdots 6$. As a zero of one of the equations of (4.6) is found the corresponding α_k is fixed and an additional parameter $\mu_k, k = 1, \cdots 6$ is freed.

In practice, it was found that this method always converged to a solution, but there is no guarantee to what solution, and a number of attempts found the trivial (zero) solution. Knowledge of an asymptotic solution can be useful in decreasing the possibility of finding the trivial solution and in speeding up the successive continuation method. Specifically we can use the asymptotics to give a good initial approximation to the projection onto the unstable eigendirections at the left hand end point. Also, knowledge of how multi-modal orbits accumulate on unimodal orbits in the unstable manifold (as in [6]), can speed up the process for locating multi-modal solutions.

In Figure 4.3 we have plotted successive results from the continuation process for the Fourier modes a_0 (a), a_1 (b), b_0 (c) and b_1 (d) at $\lambda = 1 \times 10^{-3}$. Note these are plotted over the computational domain - that is up to the symmetric section at $T = 82.5$. Curve a is the asymptotic approximation and hence corresponds to the start of the successive continuation process. Curve e corresponds to the end of the successive continuation at which $\alpha_k = 0$ for $k = 1, \cdots, 6$ and is hence the first solution which satisfies the original BVP, that is equations (2.6) and (2.7) supplemented with boundary conditions (3.4)–(3.6). This may then be used to start further computations, for example continuation in a problem parameter. Curves b–d represent intervening steps of the successive continuation as $\alpha_k = 0$ for some $k \in \{1, \cdots, 6\}$. Note that, for the sake of clarity, not all these intervening steps have been presented. It is clear from Figure 4.3 that the intervening steps, curves b–d, do not satisfy all the boundary conditions of the original BVP.

In the implementation it was on occasion necessary to reduce the length of the interval T artificially for Newton's method to converge. It was also found that a judicious choice of which parameters are free at $x = 0$ could be used to ensure that the continuation was successful. Finally recall that the successive continuation method did on occasion converge to the trivial solution.

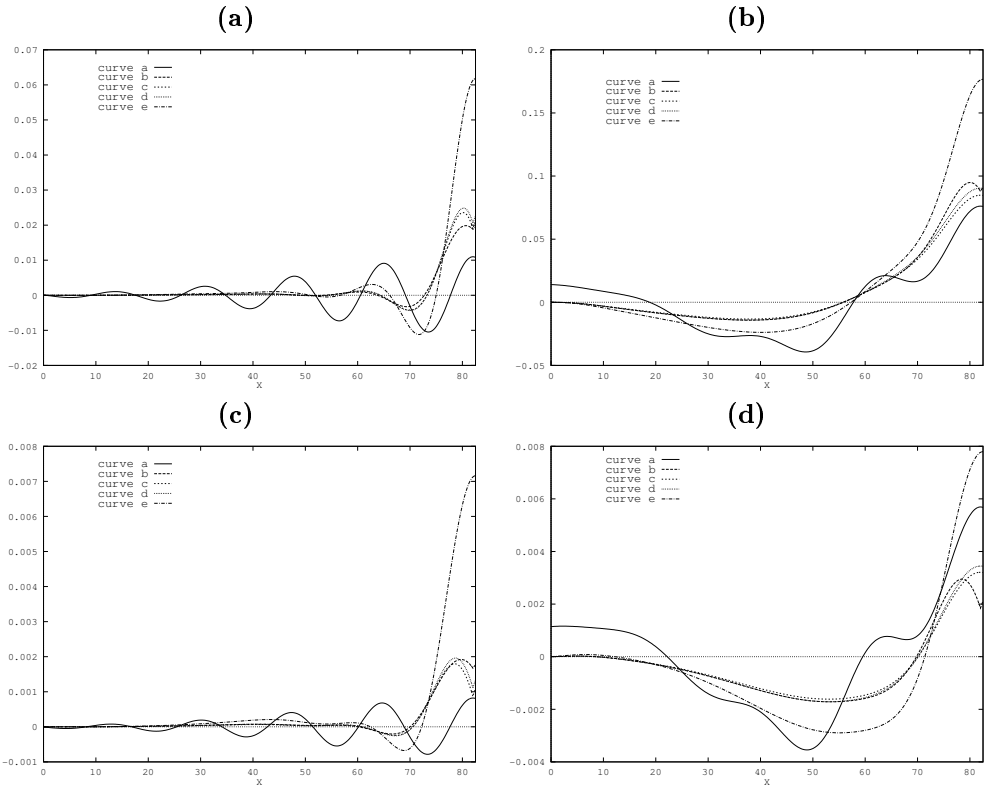

FIG. 4.3. *Fourier modes a_0 (a) , a_1 (b) for the displacement and modes b_0 (c), b_1 (d) for the stress function ϕ; plotted up to the symmetric section. Illustrates the use of successive continuation to find an initial solution for the BVP. Note that the boundary conditions are only all satisfied at start and finish of iteration. Curve a is the initial approximation from the asymptotics and curve e is the end product of the successive continuation. Curves b-d are some of the intermediate steps of the successive continuation.*

4.3. Increasing the number of modes. A naive way of increasing the number of modes used, i.e. to increase M, is to take a homoclinic solution successfully computed for $m = 0, \ldots, M-1$ and then add trivial data for the solution in the Mth mode as a starting solution for the BVP with M modes. In practice, it is found that this method is only likely to be successful if M is sufficiently large, but for small M the component of the true homoclinic solution in the Mth mode is likely to be too significant for this to work.

A more reliable method to add in extra modes, is again to used a continuation method. Specifically, a homotopy parameter $\eta \in [0, 1]$ is introduced as a factor multiplying the nonlinear terms in the added harmonic. In the notation of (2.8), suppose that a homoclinic solution has been found for U_m, $m = 0, 1, \ldots, M-1$. Then, form

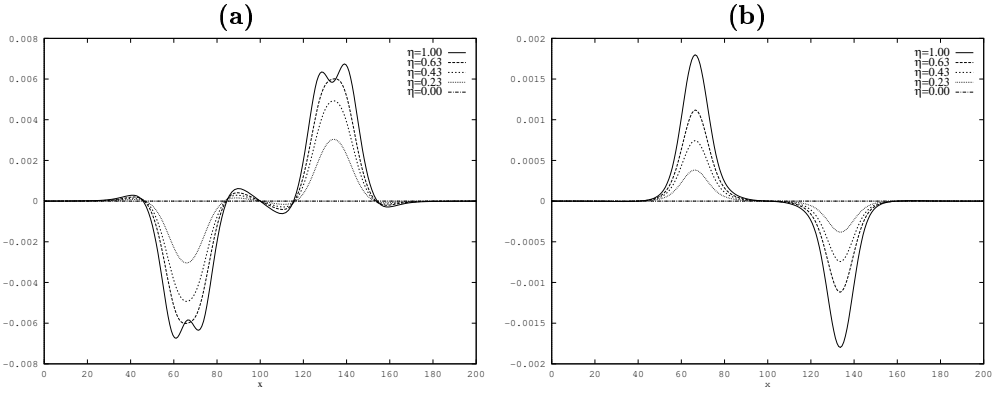

FIG. 4.4. *Homotopy used to introduce extra Galerkin modes a_3 (a) and b_3 (b). Seed mode $s = 11$. Initially the modes a_3 and b_3 are zero at $\eta = 0$ and $M = 3$, at $\eta = 1$ the new modes are fully introduced and $M = 4$.*

the system

$$U_m' = A_i U_i + F_m(U_0, \ldots, U_{M-1}, U_M), \quad m = 0, 1, \ldots, M-1 \tag{4.7}$$

$$U_M' = A_M U_M + \eta F_M(U_0, \ldots, U_{M-1}, U_M) \tag{4.8}$$

for which we seek solutions satisfying the boundary conditions (3.4)–(3.6). With $\eta = 0$, (4.8) is linear and decoupled from (4.7), and so $U_M \equiv 0$ is the unique solution satisfying the boundary conditions. Hence (4.7) is satisfied by the previous homoclinic solution computed for $M - 1$. Numerical continuation can then be used to homotopy to $\eta = 1$, whence we have a homoclinic solutions with one extra mode. This method was always found to be successful in the computations that follow, but was not always required for larger M since the BVP solver would converge directly to a solution from an initial guess with $U_M \equiv 0$ and $\eta = 1$. This is to be expected since as the number of modes is increased we expect convergence of the Galerkin approximation and the contribution in the added mode to be correspondingly small. In Figure 4.4 we show the results of this homotopy technique, used to increase from $M = 3$ to $M = 4$ for a seed of $s = 11$ (i.e. passing from $m = 0, 1, 2$ to $m = 0, 1, 2, 3$). In Figure 4.4 (a) we have plotted the Fourier mode a_3 for the displacement and in (b) we have plotted the Fourier mode b_3 for the stress function ϕ as the homotopy parameter η is continued from 0 to 1. As is clear from the figure, the example shown is for a cross-symmetric form of solution.

4.4. Altering wave-number of seed mode. Having found a solution in one particular wave number (i.e. for one particular value of s in (2.6),(2.7)) we require a method for finding a solution in a different wave number s'. To achieve this we use continuation in s, treating s as a real variable. Note that these solutions only make physical sense as solutions of (2.1),(2.2) with periodic-in-y boundary conditions, if s is an integer; a real-valued s is merely a way to be able to homotopy a solution to a new wave number. An example of such a computation is shown in Figure 4.5 in which we have plotted the maximum value of the Fourier mode a_0 of the displacement w against the seed s. This shows that, given a solution for a particular integer s, we are able to find a corresponding solution for any other integer value of s. Note that as s becomes small (approximately $s < 5$) the von Kármán–Donnell model loses validity [31].

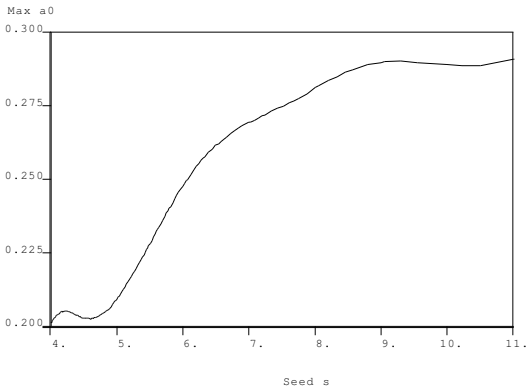

FIG. 4.5. *Continuation in the seed s. Maximum value of the Fourier mode a_0 plotted as the seed s is decreased. Recall that only integer values of s correspond to the physical problem.*

4.5. Changing boundary conditions. Finally we require a homotopy technique to change between the two types of boundary conditions: symmetric (2.10) and cross-symmetric (2.11). To achieve this we introduce a homotopy parameter η into the boundary conditions (3.5-3.6). Thus we solve the BVP described in section 3 with (3.6) replaced by

$$\left\{ \begin{array}{ll} \frac{\partial a_m(1)}{\partial x} = 0, & \frac{\partial^3 a_m(1)}{\partial x^3} = 0 \\ \frac{\partial b_m(1)}{\partial x} = 0, & \frac{\partial^3 b_m(1)}{\partial x^3} = 0 \end{array} \right. \tag{4.9}$$

for m even and

$$\left\{ \begin{array}{ll} (1-\eta)\frac{\partial a_m(1)}{\partial x} + \eta a_m(1) = 0; & (1-\eta)\frac{\partial^3 a_m(1)}{\partial x^3} + \eta \frac{\partial^2 a_m(1)}{\partial x^2} = 0, \\ (1-\eta)\frac{\partial b_m(1)}{\partial x} + \eta b_m(1) = 0; & (1-\eta)\frac{\partial^3 b_m(1)}{\partial x^3} + \eta \frac{\partial^2 b_m(1)}{\partial x^2} = 0 \end{array} \right. \tag{4.10}$$

for m odd. Thus at $\eta = 0$ the BVP solves the symmetric problem and at $\eta = 1$ it solves the cross-symmetric problem. This is illustrated in Figure 4.6 in which we have plotted the maximum value of a_0 against η as we continue from the symmetric to cross-symmetric problem. Computation was performed for a seed $s = 15$ for a 2 mode approximation ($M = 2$) at a fixed value of $\lambda = 1.3 \times 10^{-3}$. It should be noted that we do not always expect a connected path to exist between the symmetric and cross-symmetric forms of solutions parametrised by $\eta \in [0, 1]$.

5. Numerical results. Yamaki describes in [46] a series of experiments performed on clamped cylindrical shells with properties (4.1). We consider here results from the longest of such shells, length $L = 160.9$ mm. Note that even this could hardly be described as long, since its aspect ratio (length to diameter) is only $L/2R \approx 0.8$. Yamaki found buckle patterns which were both symmetric and cross-symmetric.

We compare with experiments the minimum, $W_{\min}$, and maximum $W_{\max}$, values of the displacements $w(x, y)$ at $\lambda = \lambda_m$, and the ratios

$$\lambda_m/\lambda_d, \qquad \beta = \frac{\text{axial wavelength at } \lambda_m}{\text{circumferential wavelength at } \lambda_m}$$

where $\lambda_d = 2\rho\kappa \approx 1.494912 \times 10^{-3}$ denotes the smallest value of λ at which the fundamental solution bifurcates, and λ_m is the minimum post buckling load (the

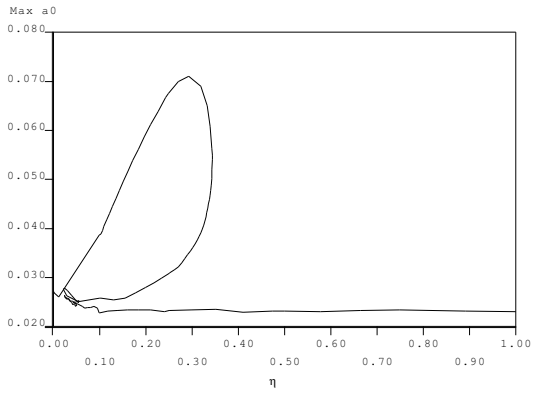

FIG. 4.6. *Continuation in the boundary conditions. Maximum value of the Fourier mode* a_0 *plotted as the homotopy parameter* η *is varied from* 0 *to* 1 *- changing the boundary conditions from a symmetric solution to cross-symmetric solution.*

first local minimum in the bifurcation diagram, see Figure 5.1). For the numerical simulations, λ_m was taken to be the first limit point on the branch of homoclinics as the loading parameter was decreased from λ_d. For the aspect ratio, β, only the axial wavelength was required from the simulations, since the circumferential wave number and hence corresponding wavelength were known. In the symmetric case the axial wavelength was defined to be the axial distance between two minima, that is the distance between the point P and Q on the contour plot Figure 5.4. In the cross-symmetric case the axial wavelength was defined to be twice the axial distance between a maximum and a minimum, that is twice the distance between the point P and Q on the contour plot Figure 5.5.

In the bifurcation diagram, Figure 5.1, we plot the load λ against a measure of the end shortening defined by the arc–length

$$\int_{-\infty}^{\infty} \sqrt{1+\left(w_x(x,y)\right)^2}\, dx = \int_{-\infty}^{\infty} \left[1+\left(\sum_{k=0}^{\infty} \frac{\partial}{\partial x}(a_k(x)\cos(ks\rho y))\right)^2\right]^{1/2} dx;$$

which in general varies with y. For simplicity we take $y = 0$ and measure over the half length of the cylinder to get,

$$\delta = \int_0^T \left[1+\left(\sum_{k=0}^{M-1} \frac{\partial a_k}{\partial x}\right)^2\right]^{1/2} dx. \tag{5.1}$$

In the computations below the half length of the cylinder T was taken to be $T = 250$, $T = 300$, or (for direct comparison with Yamaki [46]) T=100. All the initial approximations were found using the methods described in section 4. The values for λ_m $W_{\min}$, $W_{\max}$ and β were found to be essentially independent of the length of the interval T solved over in accordance with results of [4, 40] and [39]. We recall that in the figures below the length of the cylinder x is plotted on $[0, 2T]$, y is plotted on $[0, 2\pi R]$ and x, y, $W_{\min}$, $W_{\max}$ and Fourier coefficients a_k are measured in *mm*.

First we examine convergence of the numerics as the number of circumferential modes used in the approximation is increased. Results are presented for the symmetric solution in Table 5.1 and for the cross-symmetric solution in Table 5.2. In each

$s = 11$	λ_m/λ_d	β	$W_{\min}$	$W_{\max}$
M=2	0.22399	3.420	-0.706	1.471
M=3	0.27902	3.052	-0.907	1.848
M=4	0.33678	3.019	-0.663	1.576
M=5	0.32726	3.005	-0.745	1.721
M=6	0.32785	2.992	-0.765	1.754
M=7	0.32795	2.877	-0.762	1.746
M=8	0.32792	2.925	-0.762	1.747
M=9	0.32792	3.006	-0.762	1.747
M=10	0.32792	2.913	-0.762	1.747

TABLE 5.1

Symmetric case: convergence of the minimum load λ_m, ratio of wavelengths β and the minimum and maximum displacements $W_{\min}$ and $W_{\max}$ as the number of modes in the approximation is increased.

$s = 11$	λ_m/λ_d	β	$W_{\min}$	$W_{\max}$
M=2	0.15152	2.123	-0.742	1.622
M=3	0.19380	1.819	-0.946	1.959
M=4	0.23209	1.571	-1.018	2.192
M=5	0.24360	1.789	-0.839	1.919
M=6	0.24179	1.741	-0.866	1.966
M=7	0.24196	1.700	-0.869	1.973
M=8	0.24198	1.740	-0.869	1.973
M=9	0.24197	1.752	-0.869	1.972
M=10	0.24197	1.728	-0.869	1.972

TABLE 5.2

Cross-symmetric case: convergence of the minimum load λ_m, ratio of wavelengths β and the minimum and maximum displacements $W_{\min}$ and $W_{\max}$ as the number of modes in the approximation is increased.

case we compare the values of λ_m/λ_d, β, and the minimum and maximum values if the displacement $W_{\min}$, and $W_{\max}$ as M is increased. We see that $M = 6$ appears to give convergence to one decimal place in all four quantities in both cases (roughly equivalent to the accuracy of the experimental data). Another indication of convergence was that, in introducing the new harmonic from $M = 5$ to $M = 6$, the $M = 5$ solution with zero in the 6th mode was a sufficiently good approximation to enable Newton's method in AUTO to converge without the need for the homotopy technique described in section 4.3. Unless otherwise indicated, the remaining results are presented for $M = 6$ (corresponding to a system of 48 ODEs) taken as a good balance between accuracy and computational tractability.

5.1. Uni-modal solutions. In Figure 5.1 we have plotted the bifurcation diagram in (a) the symmetric case for $s = 7, 8, 9$ and 11 and in (b) for the cross-symmetric solution with $s = 8, 9, 10$ and 11. The curve of homoclinic orbits originates, in both cases, from the bifurcation point $\lambda_d \approx 1.494912 \times 10^{-3}$ on the λ axis. The limit point λ_m is at the first minimum value of the loading parameter λ along the curve originating at λ_d.

We now examine the solutions along the bifurcation branch, taking as an example the seed $s = 11$ in both the symmetric and cross-symmetric cases. In Figures 5.2 and 5.3 show the symmetric and cross-symmetric solutions respectively at the minimum

load λ_m where $\lambda_m = 4.901 \times 10^{-4}$ in the symmetric case and $\lambda_m = 3.615 \times 10^{-4}$ for the cross-symmetric case. In Figures 5.2 (a) and 5.3 (a) the Fourier modes a_0–a_5 for the displacement $w(x,y)$ are plotted and in (b) the modes b_0–b_5 for the stress function $\phi(x,y)$ are plotted. In Figures 5.2 (c) and 5.3 (c) the reconstructed displacement $w(x,0)$ is plotted and in 5.2 (d) and 5.3 (d) the stress function $\phi(x,0)$ is plotted.

Note that the contribution from the Fourier modes a_4 and a_5 is small in magnitude, and hence difficult to distinguish. However, these modes do contribute overall as can be seen from Tables 5.1 and 5.2.

In Figure 5.4 we have plotted the contour plot of the displacement $w(x,y)$ for the symmetric form of solution, plotted over the cylinder at the minimum load λ_m, with the values of certain contours marked. This solution is reconstructed from the Fourier modes in Figure 5.2. In Figure 5.5 we have plotted the identical contour plot for the cross-symmetric case of Figure 5.3. In each case the (cross-)symmetric nature of the solution over the whole cylinder is clearly evident. The circumferential wave number s is easily verified as 11. Figures 5.4 and 5.5 compare favourably with the experimental results in [46]. The 3-dimensional plot in Figure 5.6 shows the full reconstructed displacement $w(x,y)$ plotted over the deformed cylinder for the symmetric case at $\lambda = \lambda_m$. In Figure 5.7 we have plotted the corresponding stress function $\phi(x,y)$ over the deformed cylinder. Similar plots were presented in [32, Figs. 6 &7] for the cross-symmetric case. Qualitatively, all the 3-dimensional plots compare well with experimental evidence.

The form of the solutions does not vary greatly (except in amplitude) from Figures 5.2 and 5.3 as the load parameter λ is decreased from λ_d to λ_m. However, after the loading parameter λ passes through the minimum at λ_m the nature of the solution changes: see Figure 5.11, discussed in the following section.

We now consider a quantative comparison between our numerics and experimental results. Note that it was found in [32] that the aspect ratio β was sensitive to small changes in the parameter λ and so this measure is not included in the comparison. In Table 5.3 we compare for the symmetric case the experimental and fully-periodic spectral approximation results of [46] (termed "Periodic" in the table). There are 3 seed modes to compare with : $s = 7, s = 8$ and $s = 9$. We see best agreement with experiments for the largest seed $s = 9$. For $s = 7$ and $s = 8$ we appear to have poor agreement with the experiments. There are two significant factors which should be

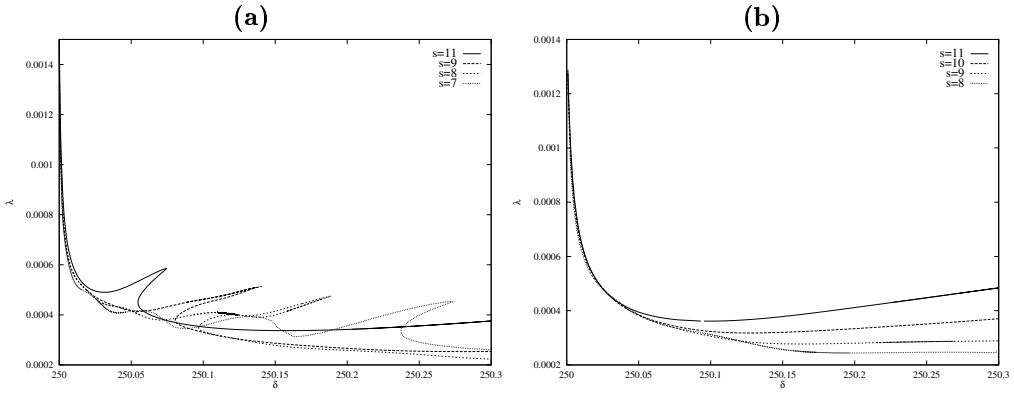

FIG. 5.1. *Bifurcation diagrams for (a) symmetric and (b) cross-symmetric solutions, for different seed modes s.*

considered.

Firstly we recall that the aspect ratio (length to diameter) ≈ 0.8 and hence the experimental cylinder is, in fact, not very long. We see from Figures 5.2, 5.4, 5.6 and 5.7 that the symmetric solutions computed appear to have a long axial wavelength and hence are, in some sense, less localized than the cross-symmetric solutions. The same phenomenon is observed experimentally as may be seen, for example, by comparing Figures 3.52e(b-f) in [46]. Thus one factor in the discrepancy may be that the experimental cylinder is too short for the symmetric form of solution and that the clamped end conditions are affecting the solution.

Secondly, consider the bifurcation diagram Figure 5.1 (a). We see that the curves flatten before the minimum λ_m occurs, particularly so for the seed $s = 7$ and $s = 8$. The same is true in the experimental case, see for example [46, Fig.3.52e(a)]. In the numerical simulations the minimum is accurately located by the limit point detection routine in AUTO, but no such routine is available for the experiments. For the seed $s = 9$, for which the minimum is easier to locate, we do achieve good agreement with the experimental data.

For the cross-symmetric case there is no such ambiguity. Table 5.4 presents a comparison with the experimental and fully-periodic spectral approximation of Yamaki [46] ("Periodic"), and with the asymptotic results of [28] in the cross-symmetric

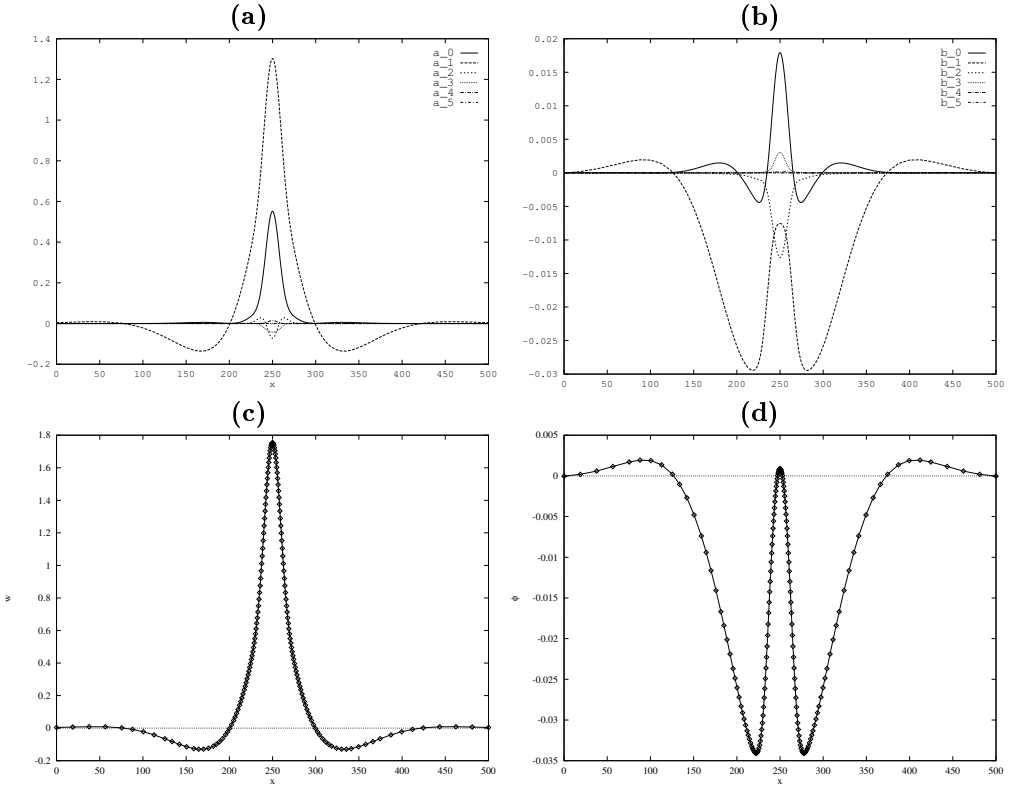

FIG. 5.2. *Symmetric form of solution at a minimum value of $\lambda = \lambda_m$. Fourier modes a_k (measured in* mm*) (a) for the displacement and modes b_k (b) for the stress function $\phi(x, y)$. In (c) reconstructed displacement $w(x, 0)$ (measured in* mm*) and (d) reconstructed stress function $\phi(x, 0)$. Solid dots represent the mesh used by* AUTO *to solve the BVP.*

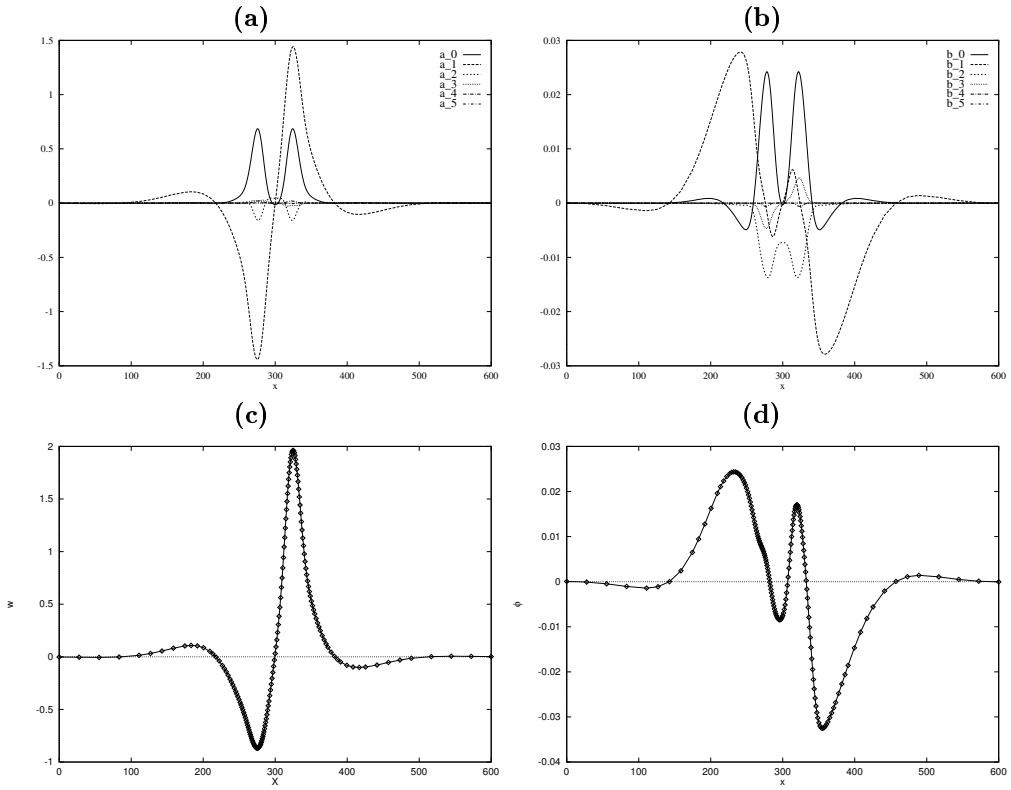

FIG. 5.3. *Cross-Symmetric form of solution at a minimum value of* $\lambda = \lambda_m$. *Fourier modes* a_k *(measured in* mm*) (a) for the displacement and modes* b_k *(b) for the stress function* $\phi(x, y)$. *In (c) reconstructed displacement* $w(x, 0)$ *(measured in* mm*) and (d) reconstructed stress function* $\phi(x, 0)$.

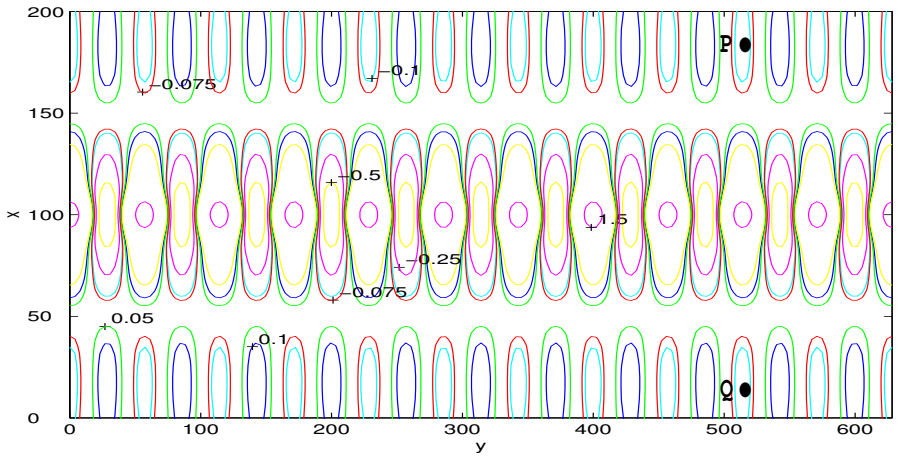

FIG. 5.4. *Contour plot for the symmetric form of solution of the outward buckling displacement* $w(x, y)$ *at the minimum value of the buckling load parameter* $\lambda = \lambda_m$.

case. For the seed modes $s = 10$ and $s = 11$ we see good agreement in the minimum load λ_m and also in the minimum and maximum displacements $W_{\min}$ and $W_{\max}$. For

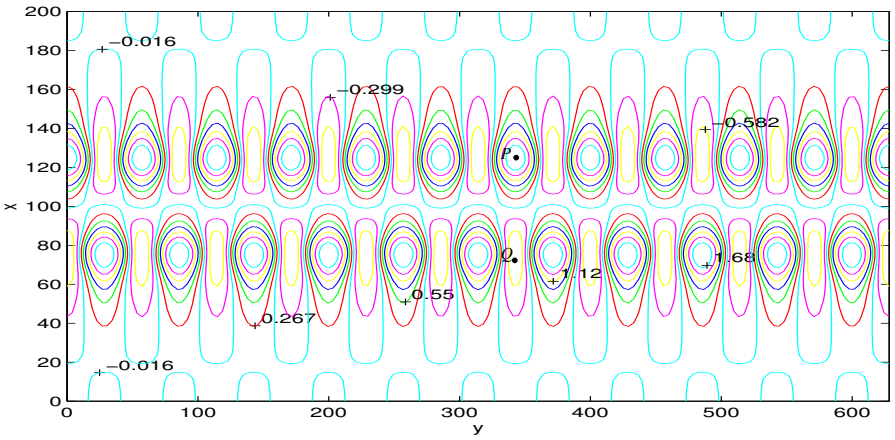

FIG. 5.5. *Contour plot for the cross-symmetric form of solution of the outward buckling displacement $w(x, y)$ at the minimum value of the buckling load parameter $\lambda = \lambda_m$.*

FIG. 5.6. *Reconstructed displacement $w(x, y)$ plotted over the deformed cylinder for $s = 11$ and $\lambda = \lambda_m$.*

the low seed numbers $s = 8$ and $s = 9$ there is a slight discrepancy in the load parameter λ_m. However these curves again are flat around the minima and hence there is some experimental error in detecting the minimum accurately.

5.2. Multi-modal solutions. The techniques described in section 4 may be used to find not only the primary or uni-modal solutions discussed in section 5.1, but also other forms of solutions. We were able to verify computationally the existence of multi-modal (cross-)symmetric solutions. The initial multi-modal solution was found from the successive continuation process (described in section 4.2) for $M = 2$, and $s = 15$ with symmetric boundary conditions. We applied the homotopy technique of section 4.5 to change the boundary conditions from symmetric to cross-symmetric. Note that owing to the sharply varying form of the multi-modal solutions it was necessary to increase the number of collocation intervals in AUTO from NTST= 20 to

FIG. 5.7. *Reconstructed stress function $\phi(x,y)$ plotted over the deformed cylinder for $s = 11$ and $\lambda = \lambda_m$.*

Symmetric Case	s	Present $M = 6$	[46] Experimental	[46] Periodic
λ_m/λ_d	7	0.273	0.13	0.17
	8	0.254	0.21	0.22
	9	0.276	0.28	0.33
$W_{\min}$	7	-0.989	-2.8	-2.49
	8	-1.477	-1.7	-1.98
	9	-1.204	-1.2	-1.48
$W_{\max}$	7	2.940	5.5	4.94
	8	3.368	4.4	3.71
	9	2.727	3.0	3.01

TABLE 5.3

Comparison of our results with experimental and traditional spectral approximation for symmetric form of the solution.

NTST= 25 or 28 [16, 17].

In Figure 5.8 we present the bifurcation diagrams for the symmetric (a) and cross-symmetric (b) multimodal solution both for seed mode $s = 15$. To obtain a clearer picture we have plotted the bifurcation parameter λ against a *measure* of end shortening given by

$$\Delta = \int_0^T \left(\sum_{k=0}^{M-1} \frac{\partial a_k}{\partial x} \right) dx.$$

Unlike the primary or uni-modal bifurcation diagrams 5.1 (a) and (b), the multi-modal solutions only exist for a limited range of parameter values. In Figure 5.9 we plot a symmetric multi-modal solution at $\lambda = 1.3 \times 10^{-3}$ with $M = 6$. In Figure 5.10 we plot a cross-symmetric multi-modal solution at $\lambda \approx 9.04 \times 10^{-4}$ and with $M = 4$. Note that the Fourier modes a_4,a_5,b_4,b_5 in the symmetric case and a_2, a_3, b_2,b_3 in the cross-symmetric case are small in magnitude and hence are difficult to distinguish on the

Cross-Symmetric	s	Present $M=6$	Present $M=10$	[46] Experimental	[46] Periodic	[28] Asymptotics
λ_m/λ_d	8	0.163	0.1563	0.14	0.12	0.16
	9	0.185	0.1840	0.17	0.17	0.18
	10	0.213	0.2123	0.21	0.22	0.21
	11	0.242	0.2419	0.24	0.26	0.24
$W_{\min}$	8	-1.894	-1.885	-1.9	-1.90	-2.15
	9	-1.411	-1.407	-1.56	-1.56	-1.68
	10	-1.075	-1.093	-1.0	-1.24	-1.36
	11	-0.866	-0.869	-0.9	-0.89	-1.09
$W_{\max}$	8	3.291	4.057	4.0	4.03	4.77
	9	2.852	3.094	3.2	3.21	3.73
	10	2.384	2.434	2.6	2.52	3.01
	11	1.966	1.972	1.9	1.90	2.47

TABLE 5.4

Comparison of our results with experimental, traditional spectral approximation and asymptotic analysis for a cross-symmetric form of the solution.

plots. Recall that this is an indication of convergence of the solution. By comparison with the symmetric uni-modal solution of Figure 5.2 and the cross-symmetric uni-modal solution of Figure 5.3 the multi–modal nature of the solutions in Figures 5.9 and 5.10 is apparent.

Finally, return to the uni-modal bifurcation diagrams of Figure 5.1. As the load λ passes through the minimum value λ_m we observe that the uni-modal solution changes in character and becomes multi-modal in nature. A similar phenomenon was observed in [6] for a simpler fourth order ODE. As an example of these multi-modal solutions we have plotted in Figure 5.11 a cross-symmetric multi-modal solution at $\lambda = 5 \times 10^{-4}$ *after* the minimum load λ_m for seed $s = 11$.

Conclusion. We have carefully described the computational aspects of computing homoclinic orbits for the von Kármán–Donnell equations. Our aim has been to illustrate carefully the steps taken in these computations and hence to describe a strategy more generally applicable to computing localized solutions in PDEs.

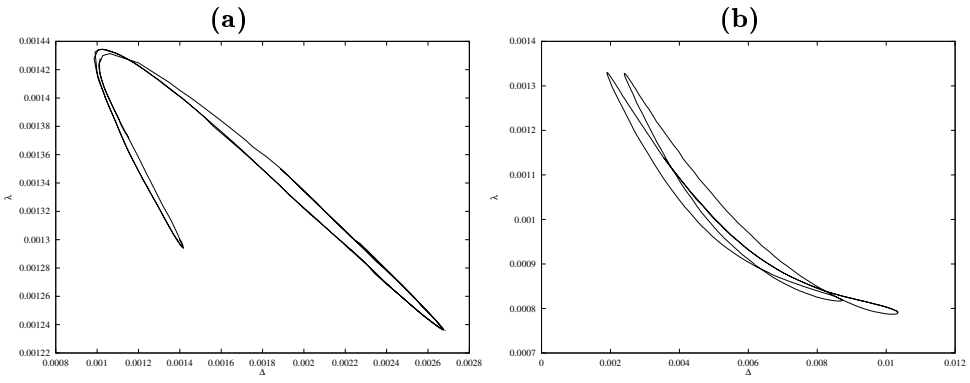

FIG. 5.8. *Bifurcation diagrams for multi-modal (a) symmetric and (b) cross-symmetric solutions, both with seed* $s = 11$.

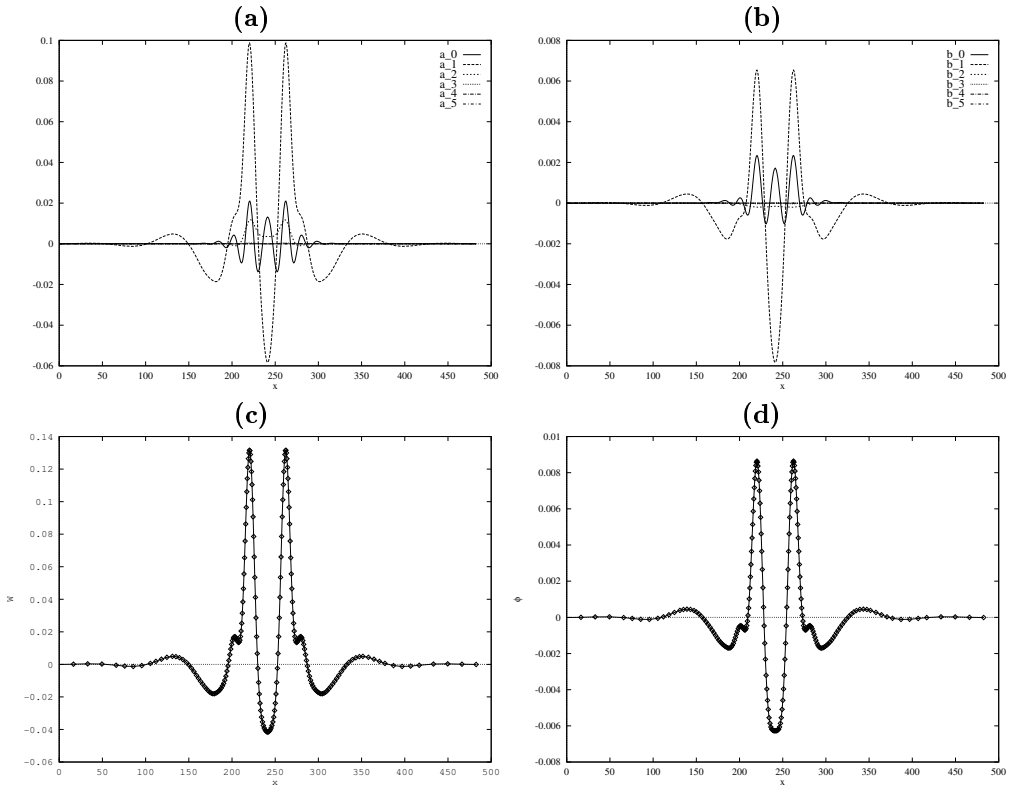

FIG. 5.9. *Symmetric form of multimodal solution at* $\lambda = 1.3 \times 10^{-3}$. *Fourier modes* a_k *(measured in* mm*) (a) for the displacement and modes* b_k *(b) for the stress function* ϕ. *In (c) reconstructed displacement* $w(x,0)$ *(measured in* mm*) and (d) reconstructed stress function* $\phi(x,0)$.

A major problem in solving for homoclinic orbits directly by a BVP, is finding an initial approximation. We have illustrated a number of practical techniques for finding initial conditions and exploited continuation to change the form of the solution. In a large system, such as that arising from the discretization of a PDE, shooting to find an initial approximation is not practical. In the case where no exact form of solution is available an asymptotic analysis may provide an approximate solution (this was of limited use for the von Kármán–Donnell equations). Failing this, the method of 'successive continuation' may be applied, which is a form of shooting as a BVP in a reduced space. This approach was illustrated using the von Kármán–Donnell equations. We applied continuation to change the symmetry in the problem (by changing the seed mode s), to increase to number of Galerkin modes circumferentially and to change the boundary conditions. Our experience has shown that a careful combination of all these techniques may be necessary for a thorough investigation.

Finally in section 5 we presented numerical results for the buckling cylinder problem and compared our results with experimental data. Qualitatively, we found good agreement for both the symmetric and cross-symmetric forms of solutions. For the symmetric form of solution there were some discrepancies between the numerical and experimental results. These may be explained by the experimental cylinder not being sufficiently long. Another factor was the experimental difficulty in determining minima accurately. No such problems were found for the cross-symmetric form of

solution: which closely matched the experiments.

Our results suggest that the buckling of a long thin axially compressed cylinder is well described by a localization theory based on homoclinic solutions. The localization occurs naturally as a solution to the von Kármán–Donnell equations, independently of any imperfections in the cylinder, and this demonstrates that the corresponding asymptotic boundary conditions are the natural boundary conditions for the computation of buckling solutions of long cylinders.

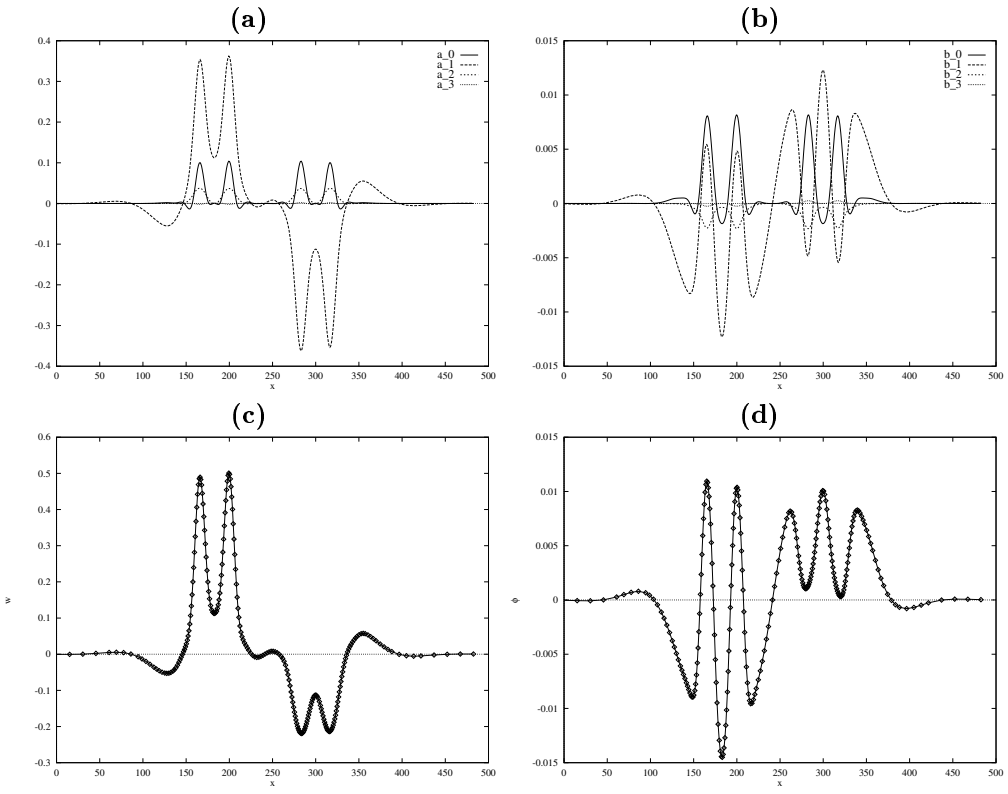

FIG. 5.10. *Cross-Symmetric form of multimodal solution at* $\lambda \approx 9.04 \times 10^{-4}$. *Fourier modes* a_k *(measured in* mm*) (a) for the displacement and modes* b_k *(b) for the stress function* ϕ. *In (c) reconstructed displacement* $w(x,0)$ *(measured in* mm*) and (d) reconstructed stress function* $\phi(x,0)$.

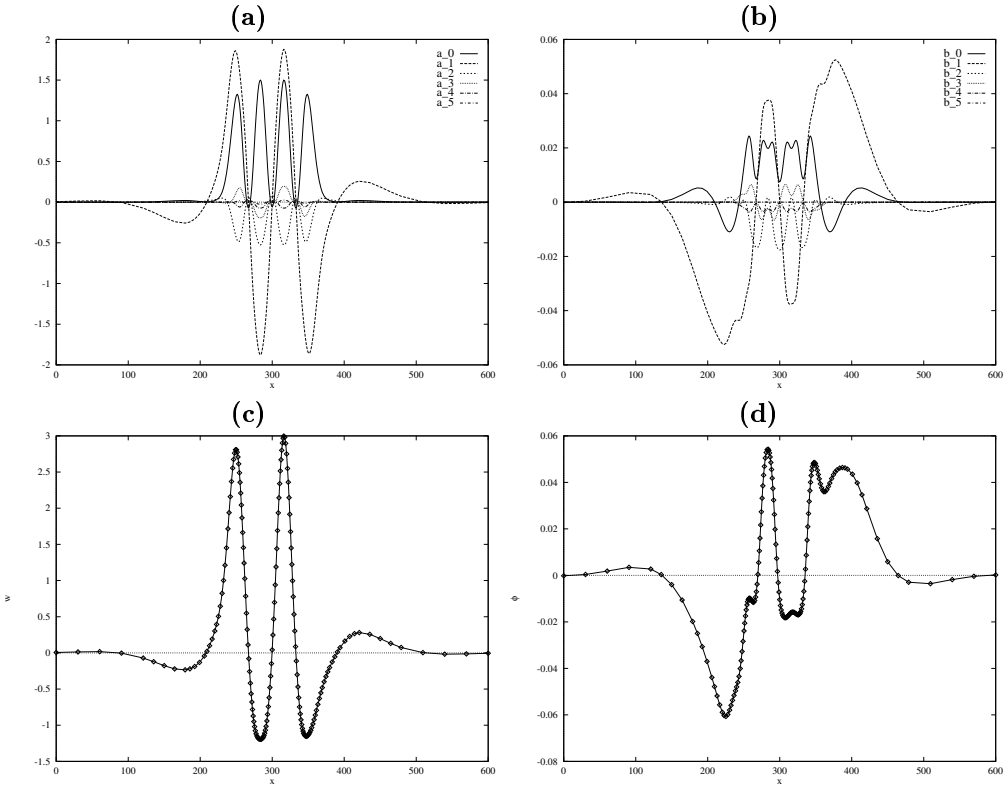

FIG. 5.11. *Cross-Symmetric form of multimodal solution at* $\lambda = 5 \times 10^{-4}$*, found after turning points on the main branch of homoclinics of Figure 5.1 (b). Fourier modes* a_k *(measured in* mm*) (a) for the displacement and modes* b_k *(b) for the stress function* ϕ*. In (c) reconstructed displacement* $w(x, 0)$ *(measured in* mm*) and (d) reconstructed stress function* $\phi(x, 0)$*.*

REFERENCES

[1] M. Ablowitz, B. M. Herbst, and C. M. Schober, *Numerical simulation of quasi–periodic solutions of the sine–Gorden equation*, Physica D, 97 (1995), pp. 37–47.

[2] F. Bai, G. Lord, and A. Spence, *Numerical computations of connecting orbits in discrete and continuous dynamical systems*, Int. J. Bifurcation and Chaos, 6 (1996), pp. 1281–1293.

[3] F. Bai, A. Staurt, and A. Spence, *The numerical computation of heteroclinic connections in systems of gradient partial differential equations*, SIAM J. Appl. Nath., (1993).

[4] W.-J. Beyn, *The numerical computation of connecting orbits in dynamical systems*, IMA Journal of Numerical Analysis, 9 (1990), pp. 379–405.

[5] ———, *On well-posed problems for connecting orbits in dynamical systems*, in Proceedings of 'Chaotic Numerics' Geelong 1993, P. Kloeden and K. Palmer, eds., AMS Contemporary Mathematics, 1993.

[6] B. Buffoni, A. R. Champneys, and J. F. Toland, *Bifurcation and coalescence of a plethora of homoclinic orbits for a Hamiltonian system*, J. Dyn. Diff. Eq., 8 (1996), pp. 221–281.

[7] S. Buonincontri and T. Hagstrom, *Multidimensional travelling wave solutions to reactio–diffusion equations*, IMA J. Applied Maths, 43 (1989), pp. 261–271.

[8] A. R. Champneys, *Subsidiary homoclinic orbits to a saddle-focus for reversible systems*, Int. J. Bifurcation Chaos, 4 (1994), pp. 1447–1482.

[9] A. R. Champneys, Y. Kuznetsov, and B. Sandstede, *A numerical toolbox for homoclinic bifurcation analysis*, Int. J. Bifurcation and Chaos, 6 (1996), pp. 867–887.

[10] A. R. Champneys and G. J. Lord, *Computation of homoclinic solutions to periodic orbits in a reduced water–wave problem*, Physica D, 102 (1997), pp. 101–124.

[11] A. R. Champneys and A. Spence, *Hunting for homoclinic orbits for autonomous Hamiltonian sytems*, Advances in Computational Mathematics, 1 (1993), pp. 81–108.

[12] R. Devaney, *Homoclinic orbits in Hamiltonian systems*, J. Diff. Eqns., 21 (1976), pp. 431–438.

[13] R. Devaney, *Reversible diffeomorphisms and flows*, Trans. Amer. Math. Soc., (1976), pp. 89–113.

[14] E. Doedel, M. Friedman, and J. Guckenheimer, *On computing connecting orbits in the sine-Gordon and Hodgkin-Huxley equatons*, IEICE Transactions on Fundamentals of Electronics, Communications and Computer Science, E77A(11) (1994), pp. 1801–1805.

[15] E. Doedel, M. Friedman, and A. Monteiro, *On locating homoclinic and heteroclinic orbits*, Appl. Math. and Comut., 65 (1994), pp. 231–239.

[16] E. Doedel, H. Keller, and J. Kernévez, *Numerical analysis and control of bifurcation problems*, Int. J. Bifurcation and Chaos, 1 (1991), pp. 493–520, 745–772.

[17] E. Doedel and J. Kernevez, *AUTO: Software for continuation problems in ordinary differential equations with applications*, Tech. Rep., California Institute of Technology, 1986. Applied Mathematics Technical Report.

[18] E. J. Doedel, M. J. Friedman, and B. I. Kunin, *Successive continuation for locating connecting orbits*, Annals of Numerical Mathematics, (1996). To appear in Special Volume on Numerical Dynamics.

[19] L. H. Donnell and C. C. Wan, *Effect of imperfections on buckling of thin cylinders and columns under axial compression*, J. of Applied Mechanics, APM-14 (1950), pp. 73–83.

[20] M. Friedman and E. Doedel, *Numerical computational of invariant manifolds connecting fixed points.*, SIAM J. Num. Anal., 28 (1994), pp. 789—808.

[21] M. Golubitsky, J. Marsden, and D. Schaeffer, *Bifurcation problems with hidden symmetries*, in Partial Differential Equations and Dynamical Systems, W. Fitzgibbon, ed., Pitman, 1984, pp. 181–210.

[22] D. Gottlieb and S. A. Orszag, *Numerical Analysis of Spectral Methods: Theory and Applications*, SIAM, Philadelphia PA, 1977.

[23] T. Hagstrom and H. B. Keller, *Asymptotic boundary conditions and numerical methods for nonlinear elliptic problems on unbounded domains.*, Math. Comp., 48 (1987), pp. 449–470.

[24] B. M. Herbst and M. J. Ablowitz, *Numerical chaos, symplectic integrators, and exponentially small splitting differences*, J. Computational Physics, 105 (1993), pp. 122–132.

[25] G. W. Hunt, *Hidden (a)symmetries of elastic and plastic bifurcation*, Appl. Mech. Rev., 39 (1986), pp. 1165–1186.

[26] G. W. Hunt, R. Lawther, and P. Providência, *Finite element modelling of spatially-chaotic structures*, Int. J. Num. Meth. Engng., (1996). To be published.

[27] G. W. Hunt and E. Lucena Neto, *Localized buckling in long axially–loaded cylindrical shells*, J. Mech. Phys. Solids, 39 (1991), pp. 881–894.

[28] ———, *Maxwell critical loads for axially loaded cylindrical shells*, Transacions of the ASME, 60 (1993), pp. 702–706.

[29] G. W. Hunt, K. A. J. Williams, and R. G. Cowell, *Hidden symmetry concepts in the elastic buckling of axially loaded cylinders*, Int. J. Solids Structures, 22 (1986), pp. 1501–1515.

[30] G. Iooss and M. C. Peroueme, *Perturbed homoclinic solutions in reversible 1:1 resonance vector fields*, J. Diff. Eq., 102 (1993), pp. 62–88.

[31] W. T. Koiter, *On the Stability of Elastic Equilibrium*, PhD thesis, University of Delft, 1945. English Translation: Tech. Rep. AFFDL-TR-70-25 Air Force Flight Dyn. Lab. 1970.

[32] G. J. Lord, A. R. Champneys, and G. W. Hunt, *Computation of localized post buckling in long axially–compressed cylindrical shells*, in Phil. Trans. Localization and Solitary Waves in Solid Mechanics, A. R. Champneys, G. W. Hunt, and M. Thompson, eds., Royal Society, 1997.

[33] R. McLachlin, *Symplectic integration of hamiltonian wave equations*, Numer. Math., 66 (1994), pp. 465–492.

[34] R. I. McLachlin, I. Szunyogh, and V. Zeitlin, *Hamiltonian finite-dimensional models of baroclinic instability*, Tech. Rep. NI96013, Isaac Newton Institute, 20 Clarkson Road, Cambridge, CB3 OEH, UK, October 1996.

[35] A. Mielke, *Hamiltonian and Lagrangian flows on center manifolds: with applications to elliptic variational problems*, Lecture notes in mathematics; 1489, Springer-Verlag, Berlin, 1991.

[36] D. Peterhof, B. Sandstede, and A. Scheel, *Exponential dichotomies for solitary–wave solutions of semilinear elliptic equations on infinite cylinders*, in Phil. Trans. Localization and Solitary Waves in Solid Mechanics, A. R. Champneys, G. W. Hunt, and M. Thompson, eds., Royal Society, 1997.

[37] E. Riks, *On the solution of mode jumping phenomena in thin walled shells*, Computer methods in applied mechanics and engineering, (1996). To Appear.

[38] E. Riks and C. C. Rankin, *Computer simulation of the buckling behavior of thin shells under quasi static loads*, in Computer Methods in Applied Mechanics, O. E. Kleiber M. and O. Zienkiewics, eds., CAM, 1996. To Appear.

[39] B. Sandstede, *Convergence estimates for the numerical approximation of homoclinic solutions*, Submitted to IMA J. Num. Anal., (1996).

[40] S. Schecter, *Numerical computation of saddle–node homoclinic bifurcation points*, SIAM J. Num. Anal., 30 (1993), pp. 1155–1178.

[41] ———, *Rate of convergence of numerical approximations to homoclinic bifurcation points*, IMA J. Num. Anal., 15 (1995), pp. 23–60.

[42] D. S. Schmidt, *Hopf's bifurcation theorem and the center theorem of Liapunov*, in The Hopf Bifurcation Theorem and its Applications, J. Marsden and M. McCracken, eds., Springer, 1976.

[43] I. Szunyogh and B. Kadar, *Truncation strategies for the two-dimensional vorticity equation*, J. Atmos. Sci., (1996). Submitted.

[44] A. I. Volpert, V. A. Volpert, and V. A. Volpert, *Traveling Wave Solutions of Parabolic Systems*, vol. 140 of Translations of Mathematical Monograpghs., AMS, Providence, USA, 1994.

[45] J. Wohlever and T. Healey, *A group theoretic approach to the global- bifurcation analysis of an axially compressed cylindrical-shell*, Computer Methods in Applied Mechanics and Engineering, 122 (1995), pp. 315–349.

[46] N. Yamaki, *Elastic Stability of Circular Cylindrical Shells*, vol. 27 of Applied Mathematics and Mechanics, Elsevier, 1984.